Applied Computing and Geosciences 8 (2020) 100036

Contents lists available at ScienceDirect

Applied Computing and Geosciences

journal homepage: www.journals.elsevier.com/applied-computing-and-geosciences

Unsupervised clustering of LA-ICP-MS raster map data for geological interpretation: A case study using epidote from the Yerington district, Nevada

Ayesha D. Ahmed [a,b,*], Shawn B. Hood [a,b,c], David R. Cooke [a,b], Ivan Belousov [a,b]

[a] Australian Research Council (ARC) Research Hub for Transforming the Mining Value Chain, University of Tasmania, Private Bag 79, Hobart, Tasmania, 7001, Australia
[b] Centre for Ore Deposit and Earth Sciences (CODES), University of Tasmania, Private Bag 79, Hobart, Tasmania, 7001, Australia
[c] GoldSpot Discoveries Corp., 69 Yonge Street, Suite, 1010, Toronto, ON, Canada

ARTICLE INFO

Keywords:
Geochemistry
PCA
Unsupervised learning
LA-ICP-MS
k-means clustering
Epidote
Ann mason
Nevada

ABSTRACT

Raster element concentration maps created using laser ablation inductively coupled plasma mass spectrometry (LA-ICP-MS) can be used to interpret microscale compositional and textural domains within mineral grains. Raster maps are typically evaluated element by element; however, application of statistical techniques (such as cluster analysis) can enhance the generation of geochemical domains to support interpretation of growth zones, core-rim relationships, sector zones, and compositional-textural associations. Clustered LA-ICP-MS map data can be assessed within individual samples and between multiple samples, and can extend insight from the microscopic scale to the regional scale to better understand geological paragenesis of an area.

Our workflow (1) applies a centred log transformation to selected elements in a raster map dataset; (2) uses principal component analysis (PCA) applied to the multi-sample, mono-mineralic dataset to group similar elements in epidote based on geochemical character; (3) applies unsupervised clustering to separate different types and generations of epidote in chemical feature space; (4) presents clustered LA-ICP-MS raster map results for interpretation of inter- and intra-mineral chemical zones; and (5) plots results spatially, across a regional map area, to investigate geological paragenesis.

The workflow is illustrated using samples of epidote from the Yerington porphyry-skarn Cu (Mo–Au) district. In the case study area, six clusters are defined by unique mineral compositions: (1) low U; (2) elevated Pb, Mn and low Fe and Sr; (3) elevated Ce, U and low Mn and Pb; (4) elevated U, Ce; low Mn, Pb; (5) elevated Sr, Fe and low Mn, Pb; and (6) elevated Mn, Sr, and Fe and low Ce and U. The regional distribution of these groups is presented as indicating proximity to the porphyry environment (lower concentrations of Ce, U, As and Sb and higher concentrations of Mn, Sr and Fe) versus retrograde skarn (elevated Ce, U, As and Sb).

1. Introduction

Laser ablation inductively coupled plasma mass spectrometry (LA-ICP-MS) is an analytical technique used to collect high-resolution quantitative geochemical data from minerals (e.g., Large et al., 2009; Ulrich et al., 2009, Cooke et al., 2014a, 2014b). Rastered lines of LA-ICP-MS spot data can be used to create 2-D geochemical maps representing elements of interest. These elemental maps are then typically used for the qualitative assessment of mineral textures and relationships (Large et al., 2009). The utility of LA-ICP-MS raster mineral maps includes interpreting magmatic history (Ubide et al., 2015), element mobility during metamorphism (Raimondo et al., 2017), hydrothermal paragenesis (Zhu et al., 2016; Román et al., 2018), relative timing of metal mineralisation (Large et al., 2009), and metallurgical prediction for ore processing (Parbhakar-Fox et al., 2016).

LA-ICP-MS element maps can contribute to the interpretation of mineral paragenesis from observed textural and geometrical features derived from inter- and intra-mineral chemical zonation. Observations are then placed into relevant geological context. However, when many elements are analysed, the number of resultant maps is high. In this case the visual comparison of pixels or patterns between maps becomes impractical because manual pattern recognition is time-consuming and

* Corresponding author. Australian Research Council (ARC) Research Hub for Transforming the Mining Value Chain, University of Tasmania, Private Bag 79, Hobart, Tasmania 7001, Australia.
E-mail address: Ayesha.Ahmed@teck.com (A.D. Ahmed).

https://doi.org/10.1016/j.acags.2020.100036
Received 16 February 2020; Received in revised form 7 August 2020; Accepted 7 August 2020
Available online 22 August 2020

evaluating the relative magnitude of chemical concentrations between regions is imprecise.

The use of unsupervised clustering to group whole-rock geochemical data for spatial analysis is well-explored (e.g., Templ et al., 2008; Campbell et al., 2009; Grunsky et al., 2014; Gazley et al., 2015; Hood et al., 2018; Sterk et al., 2018). In contrast, studies of clustering applied to *in-situ* mineral chemistry data are less common and focus on interpreting geochemical groups without an emphasis on spatial distribution (e.g., pyrite; Campbell et al., 2009; Gourcerol et al., 2018a,2018b; Román et al., 2018; Kerr et al., 2018). Lawley et al. (2020) applied cluster analysis to LA-ICP-MS map data of sulphides to assess precious metal mobility during alteration. However, PCA and cluster analysis were applied to individual samples (not multi-sample compiled data) and multi-mineral element maps (not mono-minerallic maps). Bence et al. (2014) introduced the application of Principal Component Analysis (PCA) to LA-ICP-MS data, followed by unsupervised clustering, to differentiate multi-phase assemblages of minerals for matrix-specific standard correction purposes. While novel and useful, the study did not address statistical issues inherent to compositional data (Aitchison, 1982, 1986) or the geological interpretation of resulting maps for use in interpreting regional geology or mineral deposits.

In this study, we present a workflow for interpreting geochemical relationships from log-ratio transformed and clustered LA-ICP-MS raster map data. The workflow (1) uses PCA to group covarying elements in epidote; (2) uses unsupervised clustering to separate compositions of epidote; and (3) presents a way to organise and summarise chemical domains within and between epidote using LA-ICP-MS raster maps. As a practical example, epidote samples from the Yerington district are processed to produce geochemical clusters which are then interpreted to infer mineral paragenesis. While epidote data are presented, the methodology is readily applicable to any raster mineral chemistry data.

1.1. Geology of the Ann Mason fault block, Yerington district, NV

The Yerington district, Nevada, is located approximately 100 km southeast of Reno, Nevada and is host to a range of Mesozoic ore deposits, including porphyry Cu (Mo–Au), skarn Cu and Fe-oxide Cu (Fig. 1). Mesozoic rocks in the district have been tilted up to 90° by post-mineralisation Basin and Range faults, resulting in a series of fault blocks that expose extensive vertical sections within and around the deposits (Proffett and Dilles, 1984; Dilles and Einaudi, 1992). The Ann Mason fault block provides the most laterally and vertically extensive exposures of a magmatic hydrothermal system in the district, from its roots through to its roof (Fig. 1). It includes the giant Ann Mason porphyry Cu (Mo–Au) deposit (1400 Mt @ 0.32% Cu, 0.006% Mo, 0.03 g/t Au), the smaller Casting Copper Cu skarn deposit, and other skarn deposits (Fig. 1). It also contains a mineralised and an unmineralised batholith, providing the opportunity for direct comparison between productive and unproductive magmatic-hydrothermal systems.

Copper mineralisation in the Yerington district is spatially and genetically associated with the composite Yerington batholith; a suite of high-K, calc-alkaline arc-related magmas (Dilles, 1987; Ahmed, 2019) emplaced in response to east-facing subduction beneath the western margin of North America in the Late Jurassic (Dilles, 1987; Dilles and Wright, 1988). The earliest phase of the Yerington batholith was the McLeod Hill quartz monzodiorite (169.4 ± 0.4 Ma; Dilles and Wright, 1988). It was followed closely by the Bear quartz monzonite, Luhr Hill granite and the Luhr Hill granite porphyry dykes (168.5 ± 0.4 Ma; Dilles and Wright, 1988). The Shamrock monzonite is a post-mineralisation intrusion (165.8 ± 0.4 Ma; Dilles and Wright, 1988) and is inferred to be unrelated to porphyry Cu or skarn mineralisation (Knopf, 1918; Dilles, 1987; Dilles and Wright, 1988; Ahmed, 2019).

Along with chlorite ± calcite, epidote is one of the main constituents of the propylitic alteration assemblage associated with porphyry Cu deposit formation (Gustafson and Hunt, 1975; Garwin, 2002; Sillitoe, 2010; Cooke et al., 2014a, 2014b). Epidote is stable over a wide temperature range (250–600 °C; Reyes, 1990; Frei et al., 2004; Cannell et al., 2005; Armbruster et al., 2006), and therefore can be found both near the deposit centre, in a proximal, high temperature environment, and distal to the porphyry centre, where fluids may have cooled significantly. At Yerington, epidote is part of at least three hydrothermal alteration assemblages: (1) associated with porphyry Cu mineralisation and

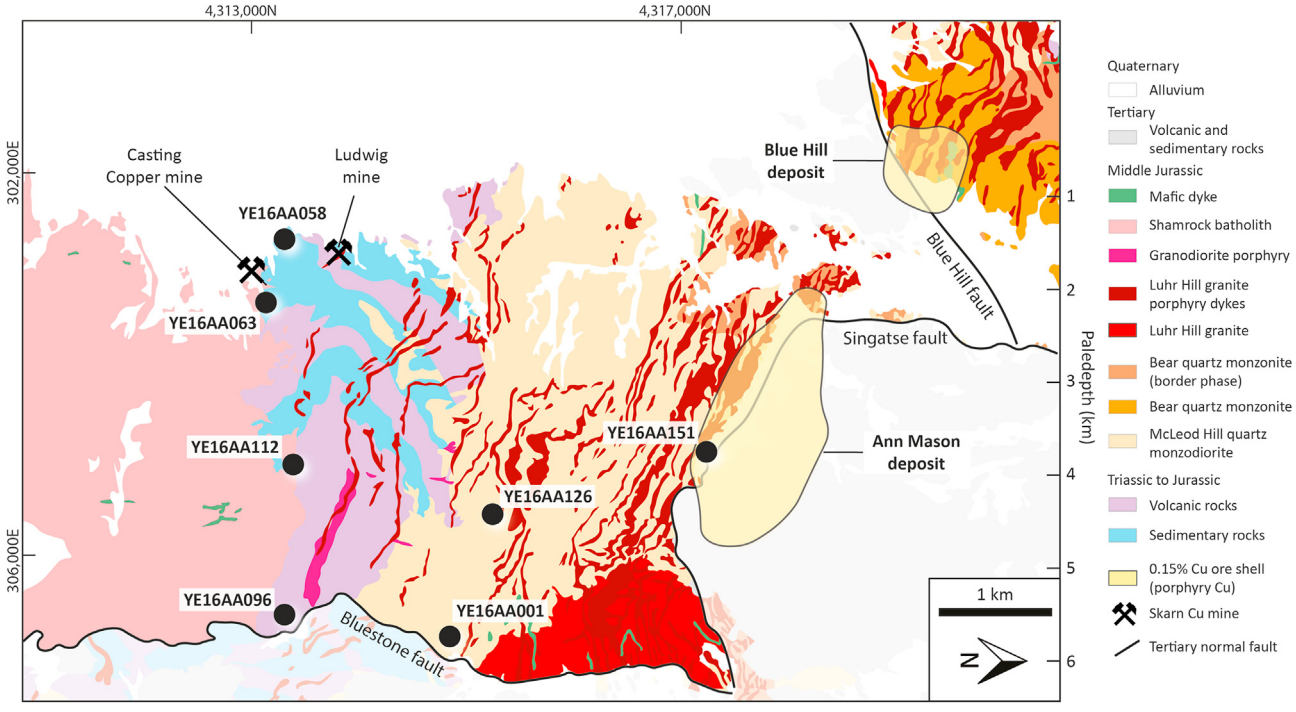

Fig. 1. Geology map of the Ann Mason fault block, modified from Proffett and Dilles (1984), showing the locations of samples used for LA-ICP-MS raster mapping of epidote. Locations and sample descriptions are included in Table 1.

emplacement of the Yerington batholith; (2) associated with retrograde skarn alteration in volcanic and sedimentary host-rocks intruded by the Yerington and Shamrock batholiths; and (3) associated with a barren hydrothermal system in the post-mineralisation Shamrock batholith. Cross-cutting relationships between these three generations of epidote are not readily observable in the field (Ahmed, 2019).

2. Methods

2.1. Sample selection and preparation

Seven samples from the Ann Mason fault block were selected for LA-ICP-MS raster mapping. Sample locations are shown on Fig. 1 and associated sample descriptions are presented in Table 1. These samples were selected to represent three features: (1) groups of alteration categorised by distance from the Ann Mason porphyry Cu deposit centre; (2) regional lithologies; and (3) different epidote-bearing vein and alteration assemblages.

All sample preparation was completed at the University of Tasmania lapidary laboratory. Samples were cut and set using epoxy into 25 mm diameter round mounts for scanning electron microscope (SEM) and LA-ICP-MS analysis.

2.2. Scanning electron microscopy

Areas of epidote for raster imaging were selected using the SEM and examined for microscale textures and major element zonation. Samples were analysed by backscattered electron (BSE) imaging and energy-dispersive X-ray spectrometry (EDS) at the University of Tasmania Central Science Laboratory using a Hitachi SU-70 Schottky field emission SEM fitted with an Oxford AZtec XMax80 silicon drift detector EDS system at 5–15 kV accelerating voltage.

2.3. LA-ICP-MS raster imaging

LA-ICP-MS raster map data were collected following the methods outlined in Ahmed et al., 2020. An Agilent 7700 ICP-MS was used coupled to an Australian Scientific Instruments Resolution system with 193 nm ArF excimer laser, housed at the CODES LA-ICP-MS Laboratory, University of Tasmania. Laser ablation analyses were performed in an atmosphere of pure He flowing at a rate of 0.35 L/min. Immediately past the ablation point within the cell, He carrier gas was mixed with Ar (1.05 l/min) for improved efficiency of aerosol transport. The ICP-MS instrument was tuned for production of molecular oxide species (i.e. $^{232}Th^{16}O/^{232}Th$) and doubly charged ion species (i.e. $^{44}Ca{+}{+}/^{44}Ca{+}$) below 0.2%, therefore no correction was applied for interfering species introduced into the analyte signal.

Images of elemental distribution within epidote grains were acquired by rastering a set of parallel lines across the sample in a grid. The laser beam size used was 4–6 μm with a repetition rate of 10 Hz, and a laser energy density of ~3.5 J/cm^2. Rastering speed was equal to the laser beam size per second. Spacing between the lines was equal to the laser beam size, resulting in full coverage of the desired area of the samples. Each line on the image was pre-ablated to remove surface contamination from previous ablations. To allow for laser cell wash-out, a delay of 20 s was used after each pre-ablation line. Time of acquisition of each image varied between 1.5 and 2.5 h, resulting in image areas of around 0.5–1 mm^2.

All samples were analysed for Fe, Al, Sr, Mn, Pb, Ce, U, Th, As and Sb. In addition to this element list, samples YE16AA001, YE16AA058, YE16AA063 and YE16AA096 were also analysed for Bi. The acquisition time for masses was 0.02–0.03 s. The total sweep time was ~0.36 s. Image data reduction followed the method outlined in Large et al. (2009) using a proprietary python script. Counts per second images were generated using background subtracted data. Conversion of counts per second images into ppm images was done using NIST610 as primary standard. This standard was analysed using a line scan, with the same spot size and scan speed as epidote samples, twice before and after each image. Aluminum was used as internal standard element. For quantification, a line of the image was chosen from an area with a clean epidote section. An Al concentration of 12 wt% was used, to approximate SEM data for epidote from chosen samples. GSD-1G, reference basaltic glass material designed by the USGS for applications to in-situ elemental analysis by LA-ICP-MS and SIMS (Jochum et al., 2008), was used as a secondary check standard.

2.4. Machine learning workflow

The workflow applied to LA-ICP-MS raster map data is presented in Fig. 2 and is modified from the methods for PCA of LA-ICP-MS spot data of pyrite outlined by Román et al. (2018) and cluster analysis of principal components by Gazley et al. (2015). Statistical analysis was undertaken using the geochemical data analysis and visualisation software IoGAS™. Data compilation was conducted in Microsoft Excel®.

2.5. Compilation of map data and filtering for epidote

LA-ICP-MS raster map data from seven maps were compiled into a single excel sheet table for statistical analysis. Compiled data were filtered for epidote using probability plots (Fe = 5 to 15 wt%). Filtered data were plotted in x-y space for visual comparison to SEM backscatter images, to ensure that all non-epidote mineral phases had been

Table 1
Sample descriptions. UTM coordinates are provided in NAD83 Zone11. Mineral abbreviations: Act = actinolite; Alb = albite; Cal = calcite; Chl = chlorite; Di = diopside; Ep = epidote; Py = pyrite; Ttn = titanite.

Sample ID	YE16AA001	YE16AA058	YE16AA063	YE16AA096	YE16AA112	YE16AA126	YE16AA151
Easting	306684	302603	303185	306516	305023	305311	304761
Northing	4314832	4313281	4312925	4314069	4313378	4315236	4317202
RL	1627	1486	1587	1653	1913	1876	1706
Sample description							
Rock unit	McLeod Hill quartz monzodiorite	McLeod Hill quartz monzodiorite (?)	Shamrock monzonite	McConnell Canyon volcanics	Shamrock monzonite	McLeod Hill quartz monzodiorite	McLeod Hill quartz monzodiorite
Visible alteration	Ep–Alb–Act–Ttn	Ep – Qtz – Cal	Ep–Di–Alb–Act–Qtz	Ep – Qtz – Cal	Ep–Alb–Act	Ep–Alb–Act–Chl	Ep–Alb
Alteration style	Patchy; clots	Pervasive	Pervasive	Pervasive	Patchy	Patchy; clots	Vein halo
Vein	–		–	–	Ep–chl	Ep–act–alb	Ep
Vein width (cm)	–		–	–	0.2	0.7	<0.1
Vein halo mineralogy	–		–	–	Ep–Alb–Act	Ep–Alb–Act	Ep-Alb–Act
Vein halo width (cm)	–		–	–	1–3	2–4	1–2
Alteration classification	Porphyry distal	Skarn	Skarn	Skarn	Shamrock	Porphyry medial	Porphyry proximal

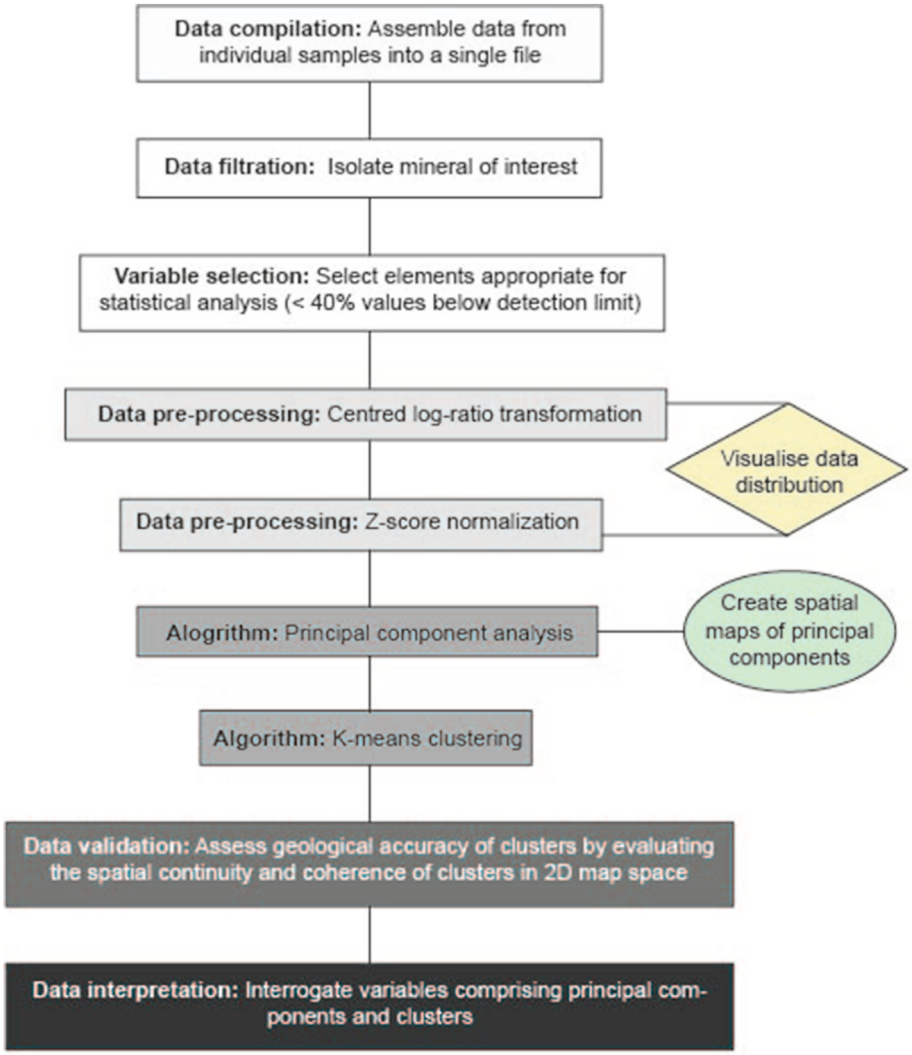

Fig. 2. Machine learning workflow applied to LA-ICP-MS raster map data from this study. Each step of the workflow is described in further detail in the text. This workflow builds on previous work by MacQueen (1967), Aitchison (1986), Templ et al. (2008), Martín-Fernández et al. (2012), Gazley et al. (2015), and Román et al. (2018).

successfully filtered out.

2.6. Modelling data distributions

Martín-Fernández et al. (2012) suggests that statistical analyses on geochemical data should only be performed on datasets where >70% of the data are above the analytical detection limit. Data distributions for LA-ICP-MS raster map data were assessed using histograms and normal score diagrams to identify variables where most data (>60%) was above the calculated analytical detection limits (Appendix A). Iron, Sr, Mn, Pb, U, and Ce were included in subsequent multivariate statistical analysis and As, Sb, Th and Bi were excluded. Variation in epidote trace element concentrations (particularly As and Sb) have been demonstrated to have a relationship with distance from porphyry deposit centres (Cooke et al., 2014a, 2014b). Therefore, univariate data of elements excluded from statistical analysis and subsequent clustering, were evaluated and integrated into final data interpretations. Aluminium was also excluded as it was used for internal concentration calibration of LA-ICP-MS analyses.

2.7. Centred log-ratio transformation and z-score normalisation

In the conversion from counts per second data to ppm space, and calibration to secondary standards, epidote mineral chemistry data were normalised to their respective oxygen-free total (98%). Therefore, compositional mineral chemistry data are closed, because they sum to a constant (in this instance 98%), and cannot be used to produce variance matrices required for PCA (Chayes, 1960). To appropriately transform compositional data, log-ratio transformations such as a centred log-ratio (CLR) can be used (Aitchison, 1982, 1986). Data were then normalised, as required before principal components analysis (Templ et al., 2008), using a z-score transformation. Normalisation removes effects of different means and measurement scales, it also facilitates comparison of spatial patterns of elements.

2.8. Principal component analysis (PCA)

Principal component analysis (PCA) uses an orthogonal transformation to convert a set of initially correlated variables to a smaller number of uncorrelated variables (Jackson, 2005). The approach reduces data dimensionality and simplifies geochemical analysis and interpretation (Grunsky et al., 2014; Gazley et al., 2015; Johnson and Wichern, 2007; Hood et al., 2018). Principal components can be used in subsequent multivariate methods such as cluster analysis and improve clustering results by helping to maximise similarity of samples and dissimilarity between clusters (Ding and He, 2004; Johnson and Wichern, 2007; Filzmoser et al., 2009). Lawley et al. (2020), Kerr et al.

(2018), and Campbell et al. (2009) demonstrated that PCA of LA-ICP-MS mineral map data improved the understanding of the relationship between textures observed in the maps and associated elements. However, neither of these studies extended to showing principal components in raster map space or geographic map space.

Classical (not robust) PCA was used to identify covarying elements associated with different compositions and generations of epidote. Only major constituents of the epidote structure (Fe, Mn, Sr, Ce, U, Pb) were used. Trace components, of which >40% of the dataset was below detection limit, were not included in the PCA. Principal component (PC) 1 accounts for the greatest variance in the dataset; PC2 the second greatest variance and so on. Results of PCA are examined as biplots, where the loadings of each principal component (i.e., the contribution of a given element to the principal component) are represented as

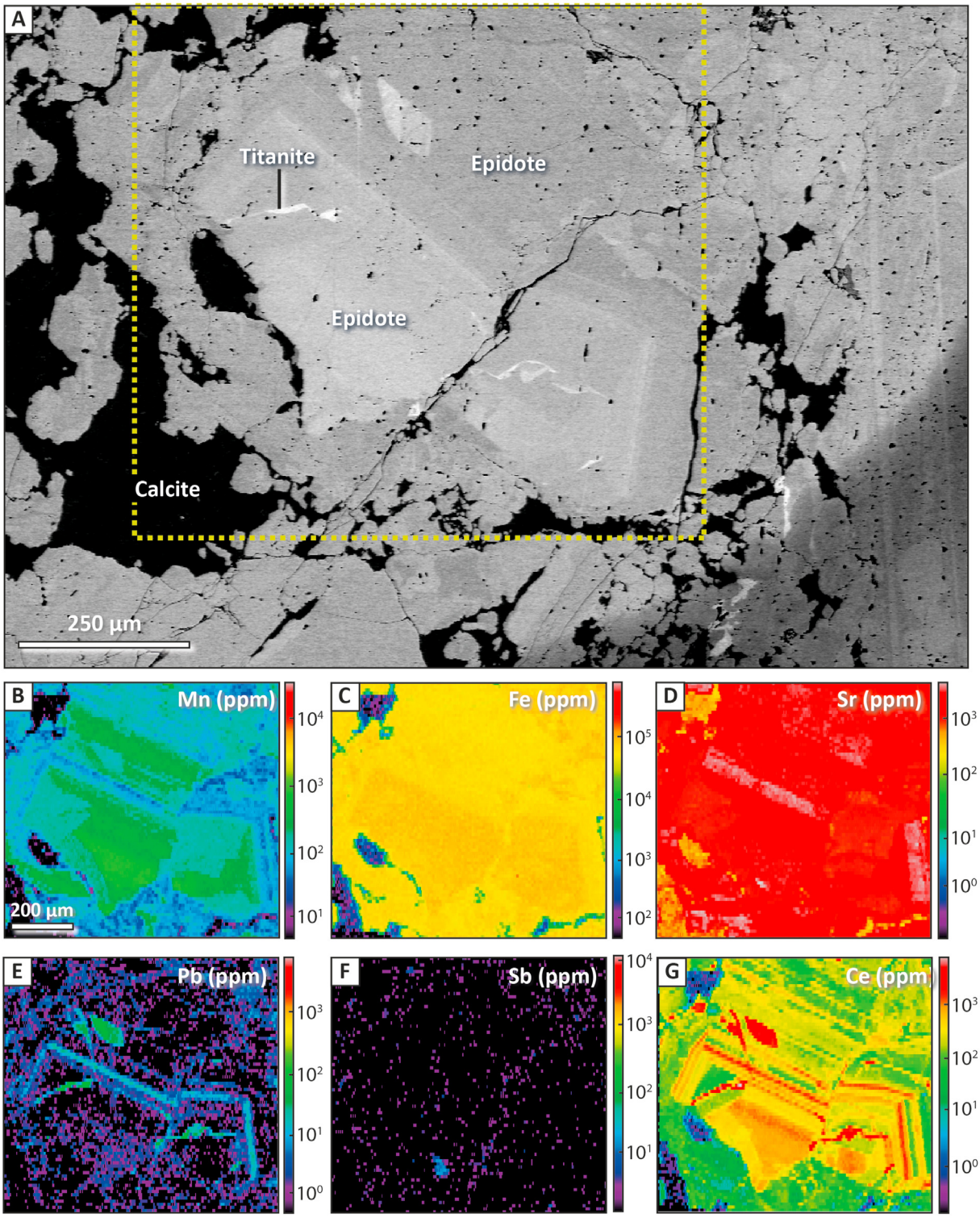

Fig. 3. SEM backscatter image and associated univariate LA-ICP-MS element maps of epidote from sample YE16AA096: A. SEM backscatter image showing location of elements maps (dashed yellow line). B. Mn; C. Fe; D. Sr; E., Pb; F. Sb; and G. Ce. LA-ICP-MS raster maps for all other samples included in this study are presented in Appendix C.

eigenvectors. The length of each eigenvector is proportional to the contribution of an element to the principal component. Long eigenvectors correspond to heavy loadings (close to 1) and indicate the principal component is strongly correlated to the given element.

2.9. Unsupervised clustering

The K-means clustering algorithm was applied to principal components in order to identify areas of similar mineral chemistry within and between samples. K-means clustering is a computationally efficient clustering method used to partition a dataset into *K* groups (MacQueen, 1967; Wagstaff et al., 2001). First, *K* initial cluster centres are selected. These clusters are then refined iteratively using the following method: (1) each data point (d_i) is assigned to its closest cluster centre using some measure of distance (e.g., Euclidean distance); and (2) each cluster centre (C_j) is updated to be the mean of its constituent instances. These steps are replicated until the location of C_j stabilises. K-means was selected as an adequate clustering method because it is widely accessible through common geochemical data manipulation platforms such as ioGAS™ and Biolabs Orange (Demšar et al., 2013).

The first three principal components were used in cluster analysis because they accounted for a majority (>90%) of the of the total variance of the dataset. The number of clusters (*K*) was determined by comparing: (1) the sum of the squares of the distances of the points from the mean of

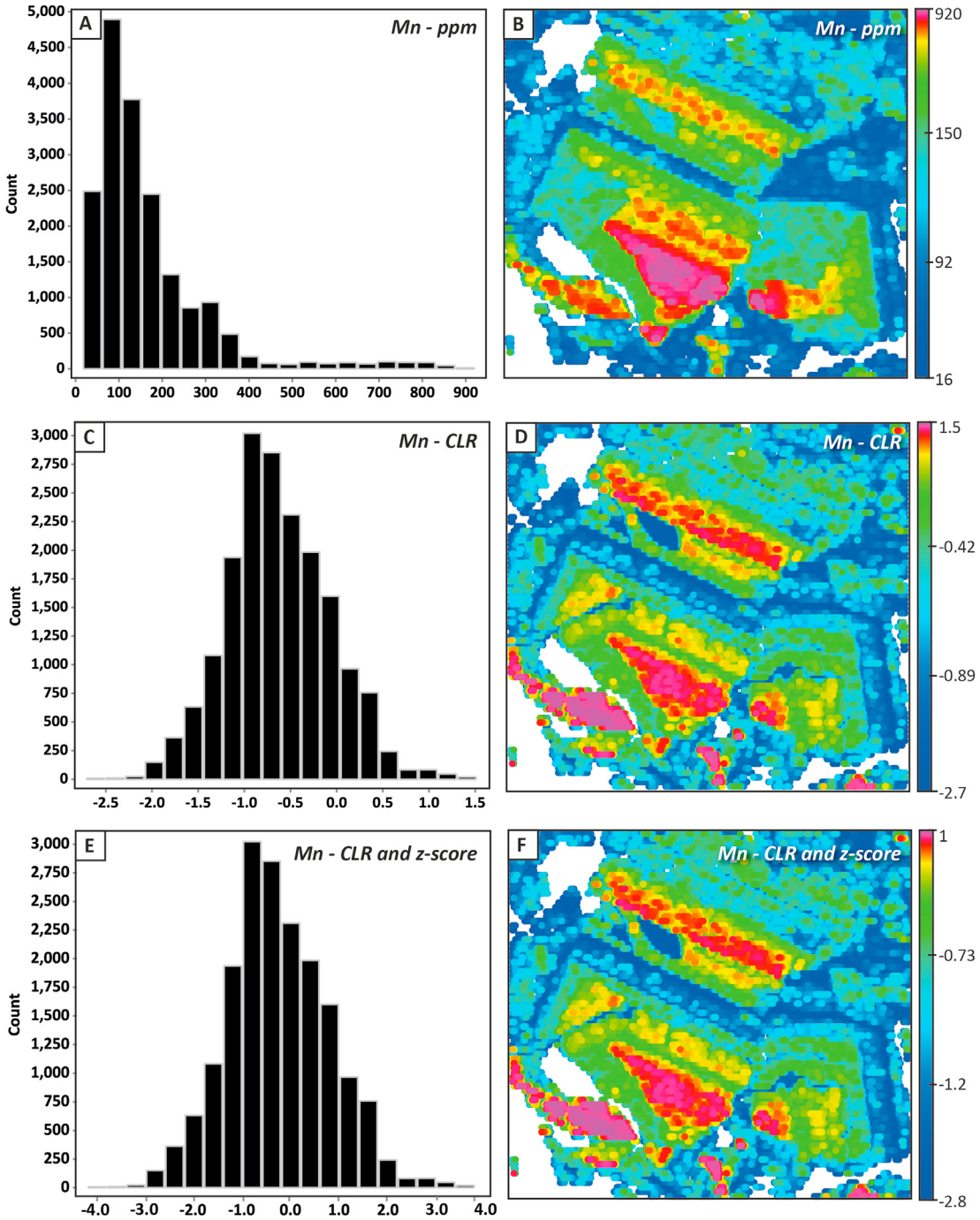

Fig. 4. Histograms (left) and ranked variable maps (right) for Mn in epidote from sample YE16AA096 showing: A – B. Untransformed ppm data. C – D. Centred log-ratio transformed data. E – F. Centred log-ratio transformed and z-score normalised data. All LA-ICP-MS raster map data are tabulated in Appendix B.

their respective clusters, to the number of clusters; and (2) the difference between the total sum of squares as the number of clusters increases.

Data clusters were evaluated in raster map space to identify areas of spatial continuity within minerals and to relate these patterns with textures observed in SEM. Clusters were also evaluated in principal component space using biplots to identify the relative contributions of principal components and individual elements to each cluster.

3. Results

Raw and processed LA-ICP-MS raster map data for all epidote samples is presented in Appendix B. Fig. 3 shows univariate LA-ICP-MS element maps generated for sample YE16AA096, along with an SEM backscatter image of the same sample location. Raster element maps for all other samples used in this study are included in Appendix C.

3.1. Data transformation

Manganese, Fe, Sr, U, Pb and Ce datasets all had >60% data above detection limits and were included in all further data transformation steps, while As, Sb, Bi and Th were excluded from further statistical analysis as <60% of the data were above analytical detection. Below detection limit data were replaced with detection limit values. An example of the data pre-processing steps from the machine learning workflow (Fig. 2) is presented for Mn in Fig. 4. Untransformed Mn ppm data has a positively skewed non-normal distribution (Fig. 4A). A CLR transformation removes the raster map data from closed compositional space (Fig. 4C). This transformation supports the interpretation of element relationships independent of correlations related to closure. A z-score normalisation applied to CLR-transformed data ensures the numeric range of all variables is the similar (Fig. 4E).

3.2. Principal component analysis

Results from the PCA are tabulated in Appendix D. Principal component 1, PC2, and PC3 account for 92% of the variability in the data. Scaled coordinates that define principal components are listed in Table 2 and are presented in Fig. 5. Large PC1 values are defined by elevated Ce and U. Conversely, low PC1 values are associated with elevated concentrations of Mn, Pb, Sr, Fe (in order of decreasing contribution; Fig. 5A – B; Table 2). Elevated Pb is the primary variable that defines large PC2 values with lesser Mn and Ce (Fig. 5B and D). Low PC2 values are associated with elevated Fe, Sr, and U (in order of decreasing contribution). Large PC3 values correspond to elevated U, Fe, and Mn (decreasing contribution), whereas small PC3 values are characterised by elevated Sr and Ce (Fig. 5C – D).

Ranked variable PC maps for sample YE16AA096 and YE16AA112 are presented in Fig. 6. Principal component maps for all other samples are included in Appendix C. In sample YE16AA096, low PC1 (Fig. 6B) and PC3 (Fig. 6D) values are associated with lower signal (darker) parts of the SEM backscatter images (Fig. 6A). Conversely, continuous zones of high PC1 – PC3 values are restricted to the higher signal (brighter) parts of the SEM backscatter image. The lowest PC1 and PC2 values are associated with a single epidote crystal, adjacent to chlorite in the centre of the image (Fig. 6F and G). Epidote twins are highlighted by positive PC3 values in an elongate epidote crystal (Fig. 6H).

3.3. Cluster analysis

The number of clusters (K) selected for K-means cluster analysis was determined based on levelling of the data trendline from the broken stick plot illustrated in Fig. 7. Shallowing of the slope (using both delta and sum of square methods; Fig. 7) is indicative of a decrease in the difference, measured in Euclidean distance space, between clusters. At lower cluster numbers, the geochemical difference between groups is highest. After some cluster number (k = n), the difference between groups does not increase and this is the natural number of discrete groups within the dataset. In the dataset from the current study, the most significant change in slope occurs where $k = 4$ (Fig. 7). However, a second change to a nearly flat slope occurs where $k = 6$. To maximise the number of features extracted from the dataset, six clusters were selected.

Principal component biplots of epidote map data coloured by cluster numbers are presented in Fig. 8. Table 2 summarises the principal element contributions to each cluster. Clusters 1, 3, 4 and 6 are largely controlled by PC1. Cluster 1 has moderate PC1 values, moderate PC2 values, and low PC3 values. This cluster is correlated with moderate values of all elements (Table 2). Cluster 6 has the overall lowest PC1 values consistent with high Mn and Pb (low Ce and U; Table 2). Clusters 3 and 4 have a similar composition in principal component space and are distinguished mainly by differences in PC2 values, consistent with Fe, Pb, and Sr content. Both clusters have high PC1 values, which corresponds to a composition dominated by U and Ce (Fig. 8; Table 2). Cluster 3 is Ce-rich with low Sr and Fe contents, whereas Cluster 4 is U-rich and has higher Sr and Fe contents. Cluster 2 is characterised by high PC2 values, which corresponds to elevated Pb and lesser Mn (Fig. 8; Table 2). Cluster 5 has the lowest PC2 values, indicative of the highest Sr and Fe contents, and with moderate values of all other elements (Fig. 8).

3.4. Chemical and textural observations

3.4.1. Yerington batholith epidote (YE16AA001, YE16AA126, and YE16AA151)

LA-ICP-MS raster maps coloured by K-means cluster are presented in Fig. 9 – Fig. 11. Fine-grained epidote in sample YE16AA001 is dominated by Cluster 1b epidote, which correlates to elevated Mn, Fe, Sr and Pb (Fig. 10C; Table 3). Coarser-grained epidote in the same sample has

Table 2
Scaled PCA stuff Ranked eigenvalue table showing the contribution of elements to principal component eigenvectors.

Scaled coordinates											
PC1		PC2		PC3		PC4		PC5		PC6	
Mn	-0.87	Fe	-0.77	Sr	-0.36	Mn	-0.32	Fe	-0.29	Ce	-3.03E-08
Pb	-0.77	Sr	-0.69	Ce	-0.29	Ce	-0.17	Ce	-0.13	Pb	-2.56E-08
Sr	-0.59	U	-0.35	Pb	0.04	Fe	-0.12	Pb	-0.13	U	-2.41E-08
Fe	-0.52	Ce	0.17	Mn	0.11	Sr	0.13	Sr	0.18	Mn	-1.85E-08
U	0.85	Mn	0.29	Fe	0.18	U	0.13	U	0.18	Sr	-1.19E-08
Ce	0.92	Pb	0.55	U	0.33	Pb	0.29	Mn	0.20	Fe	-1.05E-08

mixed patches of Cluster 1a and Cluster 1b (Fig. 10C). Conversely, samples YE16AA126 and YE16AA151 have dominantly Cluster 1a epidote with minor amounts of Cluster 2a and Cluster 1b epidote. Geochemical differences between fine and coarse-grained epidote were not well-developed in these samples.

3.4.2. Retrograde skarn epidote (YE16AA058, YE16AA063, and YE16AA096)

All three retrograde skarn epidote samples have minor amounts of Cluster 1a, which has moderate concentrations of all elements (Table 3). The zonation of coarse-grained epidote in samples YE16AA058 and YE16AA063 has been assigned to Cluster 2c, which is correlated with high U and low Pb and Mn values (10B–C; Table 3). The margins of coarse-grained epidote in both samples are rimmed by a thin band of Cluster 2b composition characterised by high Ce and lesser U (Table 3). Fine-grained epidote in samples YE16AA058 and YE16AA063 has been assigned to Cluster 2a, which has high Sr and Fe, and low Mn, Pb, Ce, and U (Table 3). Coarse-grained epidote in sample YE16AA096 has been assigned to Cluster 2b, which is characterised by high Ce values and moderate U (Table 3). This is the same composition as the rims that formed on the edges of coarse-grained epidote in YE16AA058 and YE16AA063 (Fig. 10B – C).

3.4.3. Shamrock batholith vein-hosted epidote (YE16AA112)

The majority of epidote in sample YE16AA112 has been assigned to Cluster 3, which corresponds to high Pb and Mn (Fig. 11; Table 3). This sample also contains a large patch of Cluster 1b epidote with high Mn, Fe, Sr and Pb (Table 3).

3.4.4. Trace element abundance

Box and whisker plots of selected samples for univariate Sb, As, Bi, and Th data (ppm), coloured by K-means cluster are presented in Fig. 12. These elements were excluded from data transforms and subsequent machine learning algorithms due to an excessive number of below

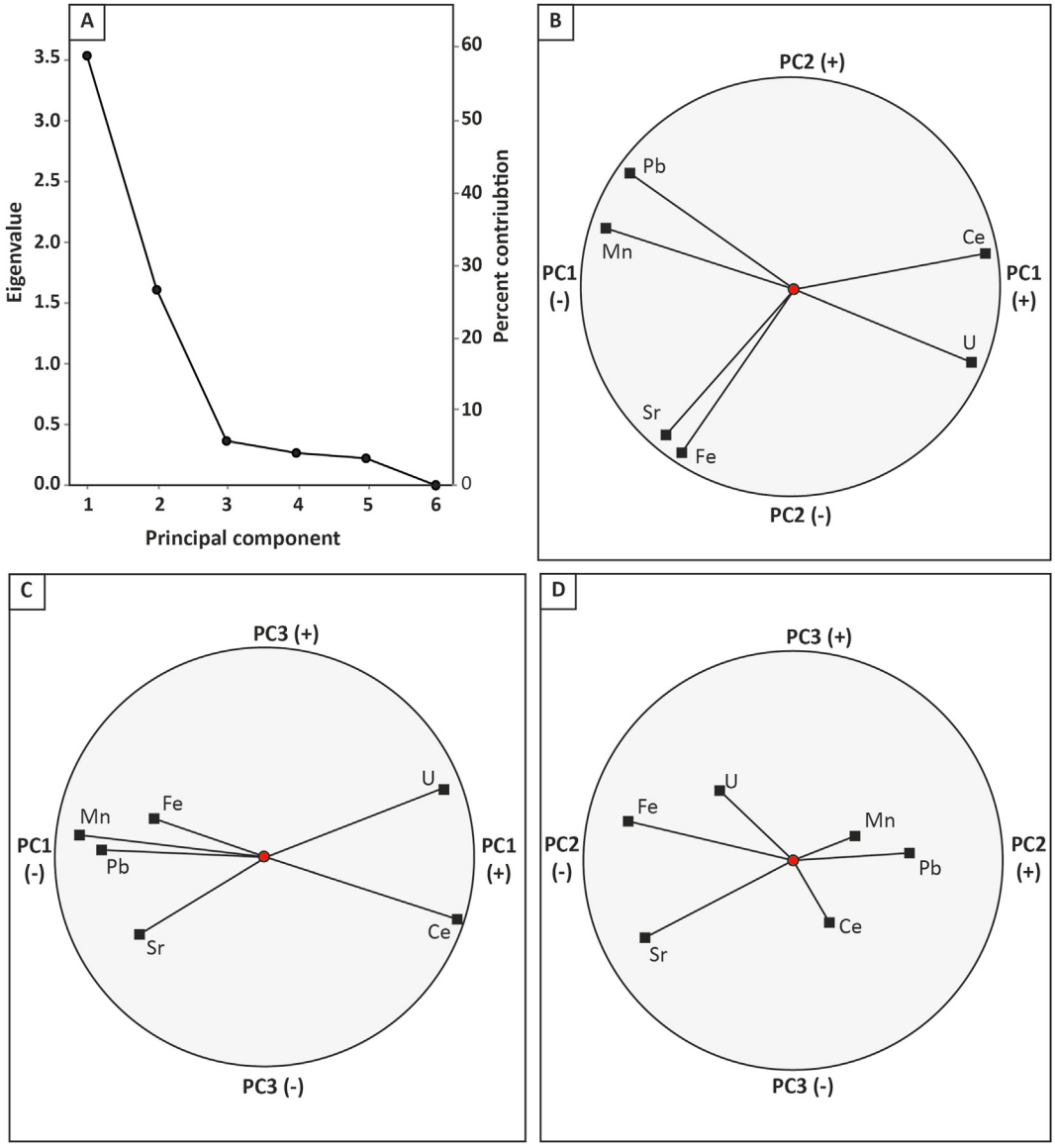

Fig. 5. Results from the principal component analysis: A. Broken stick plot showing the total sum of eigenvalues vs the number of principal components, and the percent contribution to principal component analysis of each component. B. Scaled coordinate values for PC1 vs. PC2. C. Scaled coordinate values for PC1 vs. PC3. D. Scaled coordinate values for PC2 vs PC3. Scaled coordinates are tabulated in Table 3. Results from this PCA are tabulated in Appendix D.

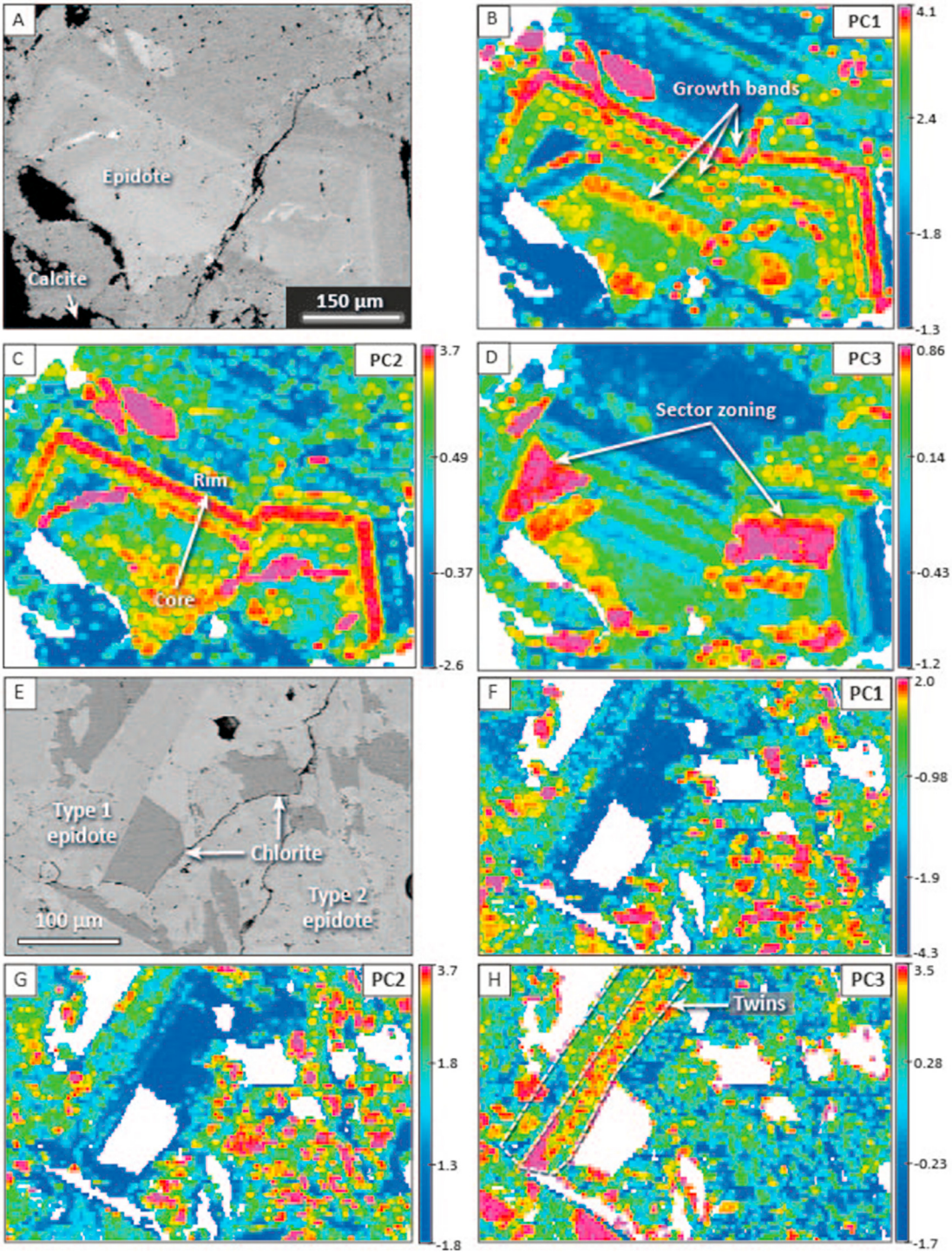

Fig. 6. Ranked variable maps of PC1, PC2, and PC3 calculated from LA-ICP-MS raster maps: A–D: YE16AA096. A. SEM backscatter image showing location of map data. B. High PC1 values record growth zoning, and low PC1 values record a different generation of epidote. C. PC2 values record changes in compositions from the core of an epidote crystal to the rim. D. High PC3 values are inferred to highlight sector zoning. E–H: YE16AA112. E. SEM backscatter image showing location of map data. F. High PC1 values are associated with fine grained epidote and low PC1 values are associated with coarse-grained epidote. G. High PC2 values are associated with fine-grained epidote. Low PC2 values are largely restricted to one zone of coarse-grained epidote adjacent to chlorite. H. High PC3 values are inferred to highlight simple twins in a coarse-grained epidote crystal. PCA maps for all other samples in this study are included in Appendix C.

detection values (>40%). High values of these elements are defined here as the upper 5th percentile of the univariate dataset measured in ppm (Fig. 12). High concentrations of As and Sb values occur dominantly in cluster 2b and 2c (with elevated U) and to a lesser degree cluster 3 (elevated Mn and Pb; Fig. 12). Clusters 1a and 3 contain most of the high Bi values, although Bi was only analysed in three samples. All the highest Th values occur in cluster 2b and 2c (elevated U and Ce; Fig. 12).

4. Discussion

Microscale textures and compositional features are routinely interpreted from LA-ICP-MS raster element maps, e.g., changes in mineral

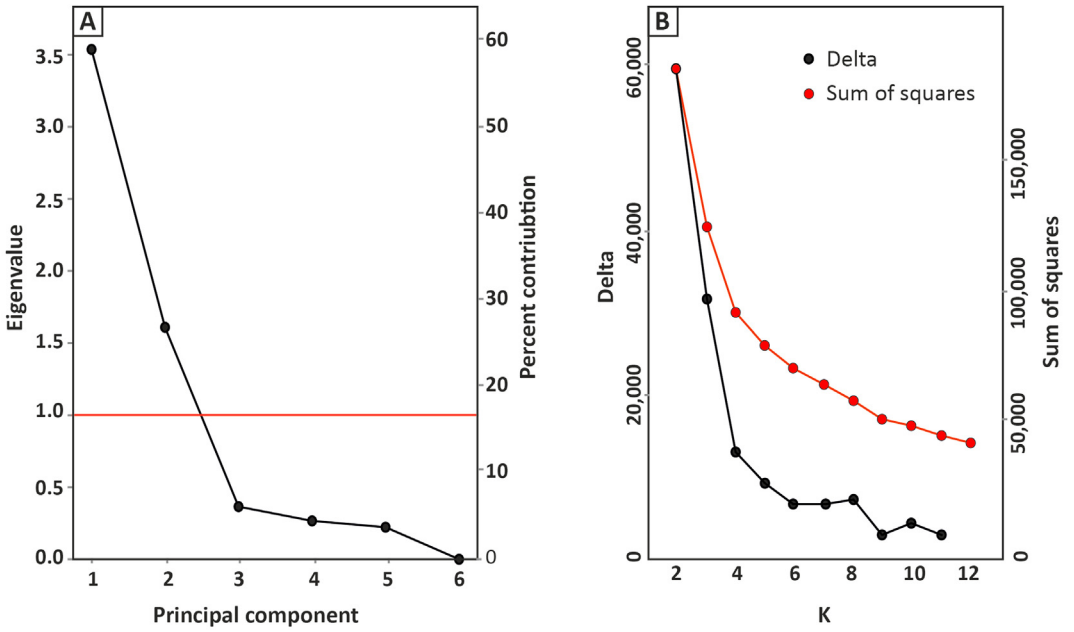

Fig. 7. Broken stick plot showing the sum of the squares of the distances of the points from the mean of their respective cluster groups (sum of squares; red) and the difference between the total sum of squares as the number of groups increases (Delta; black).

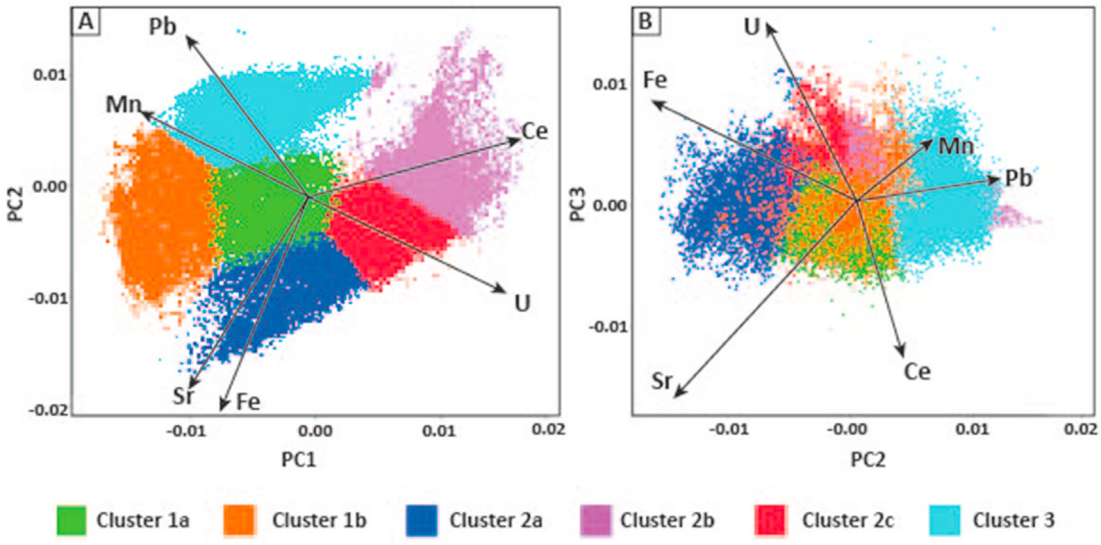

Fig. 8. Principal component biplots of all epidote LA-ICP-MS raster map data showing the geochemical relationship between different elements comprising each principal component. A. RQ2 vs. RQ1. B. RQ3 vs. RQ2. Data is coloured by K-means cluster. Results from this PCA are tabulated in Appendix D.

composition associated with growth zones, lamellar zones, twins, microfractures, and micro-inclusions (e.g., Román et al., 2018; Large et al., 2009; Cooke et al., 2014b; Kerr et al., 2018). However, to assess all analysed elements using univariate maps requires many maps to be produced. As the number of univariate maps increases, it becomes more difficult to visually inspect for patterns, contrasts, or statistical correlation of elements between images. Furthermore, it is difficult to represent qualitative observations from univariate LA-ICP-MS raster maps in geographic space.

Understanding the macro-scale geological significance of compositional clusters generated using the LA-ICP-MS workflow depends on placing micro-scale observations into the geological context of the rock samples. First, the clusters should be considered in terms of geochemical similarities and differences. These can be related to individual mineral paragenesis and general geochemical characteristics of an area. Secondly, the presence of relative abundance of clusters can be plotted for each rock sample, in geographic space, and considered relative to regional paragenesis. These two aspects are discussed below using the Ann Mason epidote samples to illustrate practical application.

In the present case study, the resultant epidote clusters represent domains of geochemical similarity or difference which relate to porphyry or skarn alteration assemblages in the Ann Mason Cu (Au–Mo) district. These quantified raster map domains (Figs. 9–11) provide a basis for comparing zonation within and between epidote samples. Elements which characterise each cluster (ether positively or negatively correlated) provide indications of geochemical affinity and can be related to mineral paragenesis. The relative proportions of epidote clusters in each sample are mapped into geographic space (Fig. 13B) as a means to spatially compare map patterns to a generalised paragenetic sequence (Fig. 13A).

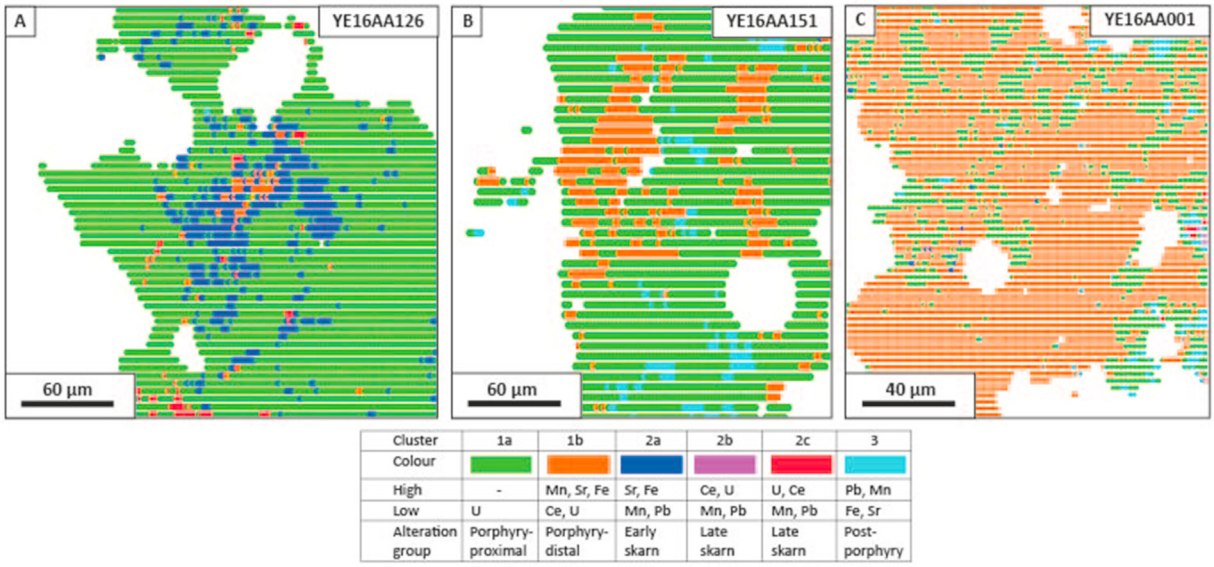

Cluster	1a	1b	2a	2b	2c	3
Colour						
High	-	Mn, Sr, Fe	Sr, Fe	Ce, U	U, Ce	Pb, Mn
Low	U	Ce, U	Mn, Pb	Mn, Pb	Mn, Pb	Fe, Sr
Alteration group	Porphyry-proximal	Porphyry-distal	Early skarn	Late skarn	Late skarn	Post-porphyry

Fig. 9. LA-ICP-MS raster maps of samples from the Yerington batholith coloured by K-means cluster: A. YE16AA126; B. YE16AA151; and C. YE16AA001. All three samples contain epidote that belong to Clusters 1a and 1b, which correspond to elevated Mn, Sr, and Fe (in order of decreasing abundance).

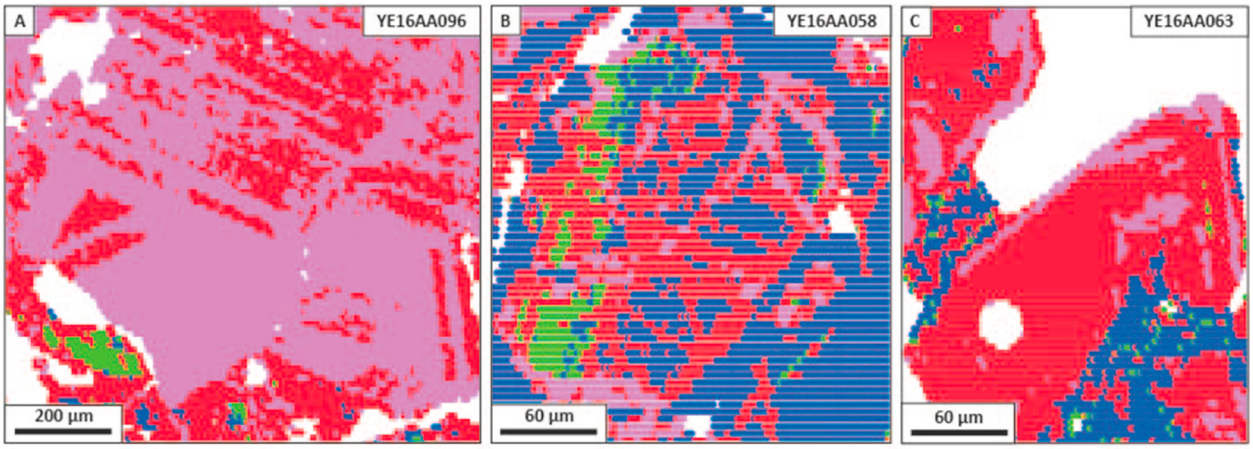

Cluster	1a	1b	2a	2b	2c	3
Colour						
High	-	Mn, Sr, Fe	Sr, Fe	Ce, U	U, Ce	Pb, Mn
Low	U	Ce, U	Mn, Pb	Mn, Pb	Mn, Pb	Fe, Sr
Alteration group	Porphyry-proximal	Porphyry-distal	Early skarn	Late skarn	Late skarn	Post-porphyry

Fig. 10. LA-ICP-MS raster maps of samples from the skarn environment coloured by K-means cluster: A. YE16AA096; B. YE16AA058; and C. YE16AA063. All three samples contain significant amounts of clusters 2a and 2b, which correlate to high U and Ce contents.

Interpreting the geochemistry and spatial relevance of LA-ICP-MS raster map clusters of epidote from the Yerington District.

To build a geographic interpretation of cluster relevance, the chemistry of epidote clusters must first be considered. Compositional variability between clusters (Table 3) produced using samples from the Yerington batholith are inferred to be a product of their location relative to the centre of Ann Mason. Clusters 1a, 1b and 2a and are inferred to reflect porphyry-related epidote compositions with elevated concentrations of Mn, Sr and Fe and the absence of significant concentrations U, Ce, As, Sb, or Bi compared to other clusters. Epidote clusters 2b and 2c are restricted to the skarn environment, in retrograde skarn assemblages dominated by epidote, actinolite or tremolite, and calcite. These clusters are characterised by high U, Ce, As, and Sb compared to other clusters and distinctly lower concentrations of Mn and Pb.

At the time of porphyry Cu mineralisation, the primary locus of heat was in the Luhr Hill cupola and around the Ann Mason porphyry dyke swarm in the Yerington batholith (Dilles and Einaudi, 1992). The univariate concentration of Mn is higher in the deposit distal sample (YE16AA001) compared to the proximal sample (YE16AA151). This difference is likely related to the decreasing solubility of Mn in the magmatic-hydrothermal fluid with distance from the deposit centre, associated with a decrease in fluid temperature (Hemley and Hunt, 1992). This interpretation is consistent with the behaviour of Mn, in both whole-rock and epidote mineral data, as a distal pathfinder element in the porphyry environment (Cooke et al., 2014a,b). Protolith composition is considered not to be a controlling the variability of Mn-content in epidote from the Yerington batholith, because all three samples are from the relatively geochemically homogenous McLeod Hill quartz monzodiorite.

In the skarn environment, fluid-rock ratios are inferred to be

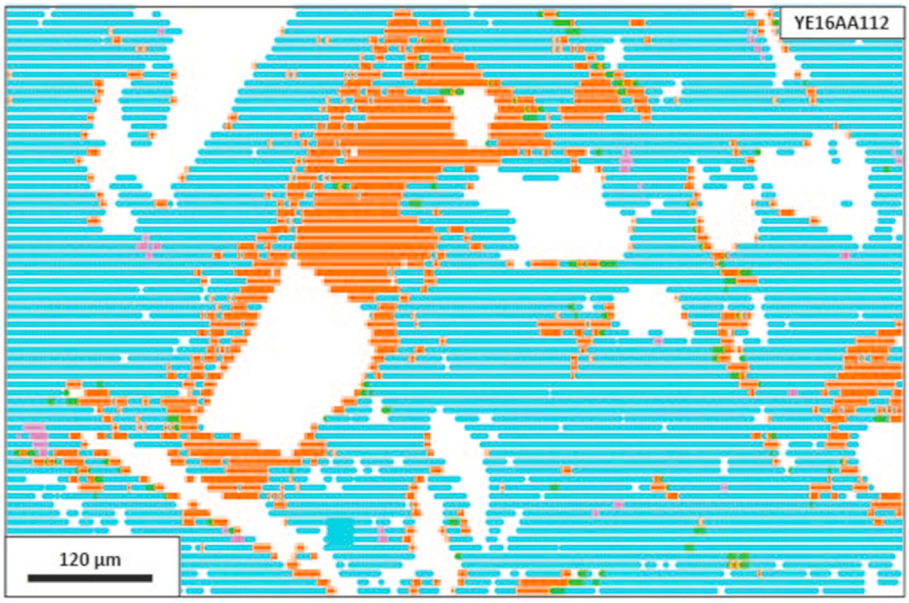

Fig. 11. LA-ICP-MS raster map of sample YE16AA112 coloured by K-means cluster. This sample contains dominantly Cluster 3 epidote with lesser Cluster 1b epidote. These compositions are consistent with elevated Pb and Mn, with lesser Sr and Fe.

Table 3
Summary of element enrichment or depletion by cluster.

	High	Low
Cluster 1	–	U
Cluster 2	Pb, Mn	Fe, Sr, U
Cluster 3	Ce, U	Mn, Pb, Sr, Fe
Cluster 4	U	Mn, Fe
Cluster 5	Sr, Fe	Mn, Pb, Ce, U
Cluster 6	Mn, Sr, Fe	Ce, U

relatively higher and thus control composition more strongly, based on the similarity in epidote composition between three highly contrasting rock types (YE16AA096: andesite; YE16AA063: monzonite; YE16AA058: limestone). Clusters 2b and 2c are spatially related to the wedge of Triassic – Jurassic volcanic and sedimentary rocks in the Ann Mason fault block (Fig. 13B). Arsenic (and Sb) values of least-altered Jurassic igneous rocks in the Yerington district are low (0.3–3 ppm; Ahmed, unpublished PhD data), similar to average crustal abundance values (Rudnick and Gao, 2014). Least-altered samples of carbonaceous argillite are absent from published whole-rock geochemical datasets for Yerington sedimentary rocks (e.g., Dilles, 1987; Proffett and Dilles, 2008). However, As and Sb can be enriched in clay-rich sedimentary rocks such as the silty limestones and argillites that dominate the upper sequence of Triassic – Jurassic rocks in the Ann Mason fault block. Global compilations of trace element data for organic-rich argillites and black shales indicate average As values between 29 and 69 ppm, an order of magnitude greater than local igneous rocks (Huyck, 1989; Quinby-Hunt et al., 1989). Therefore, leaching of As and Sb from sedimentary host rocks may explain the elevated values of these elements in retrograde skarn epidote compared to epidote from the Yerington batholith.

Cluster 2b, retrograde skarn epidote, contains high Ce values nearing allanite composition (up to 1% Ce, Appendix B). Allanite is a common component of skarn assemblages (e.g., Papunen and Lindsjö, 1972; Pan and Fleet, 1990; Smith et al., 2002). The highest Ce values are concentrated in alternating growth bands of high and low Ce-contents (YE16AA063 and YE16AA096; Figs. 4, 7 and 10) and in microfractures that transect epidote grains (YE16AA058; Appendix C).

4.1. Defining paragenetic relationships from epidote raster map clusters

In peripheral locations around ore deposits, such as the distal porphyry environment at Ann Mason, obvious paragenetic relationships such as crosscutting veins between different generations of a mineral can be absent. This issue prevents the interpretation of relative timing between hydrothermal events, and absolute timing cannot be resolved using conventional geochronology techniques (i.e., Ar–Ar, U–Pb, and Re–Os) due to a lack of precision (Chiaradia et al., 2013). High resolution LA-ICP-MS raster maps do allow interpretation of relative timing because at small scale, cross cutting relationships and intergrowths can be observed (Large et al., 2009).

Two samples from the retrograde skarn environment contain cluster 2a epidote. In sample YE16AA096, cluster 2a epidote is crosscut by clusters 2b and 2c, which occur as fracture infill. For this reason, we infer cluster 2a to have formed early relative to clusters 2b and 2c. Given that cluster 2a was also present in porphyry-related epidote, it is possible that this cluster may represent an early prograde phase of the mineral.

Epidote from the Shamrock batholith is characterised dominantly by cluster 3 epidote, containing elevated concentrations of Pb and Mn. Cluster 3 epidote only occurs in a significant amount within the Shamrock monzonite, which was emplaced after the Yerington batholith and is inferred to post-date both skarn and porphyry-style mineralisation in the district (Dilles, 1987; Dilles and Wright, 1988). As such cluster 3 epidote is inferred to be late in the paragenetic sequence (Fig. 13A). The Pb and Mn concentrations of least-altered samples from the Yerington and Shamrock batholiths are similar (<10 ppm Pb; 200–300 ppm Mn; Ahmed

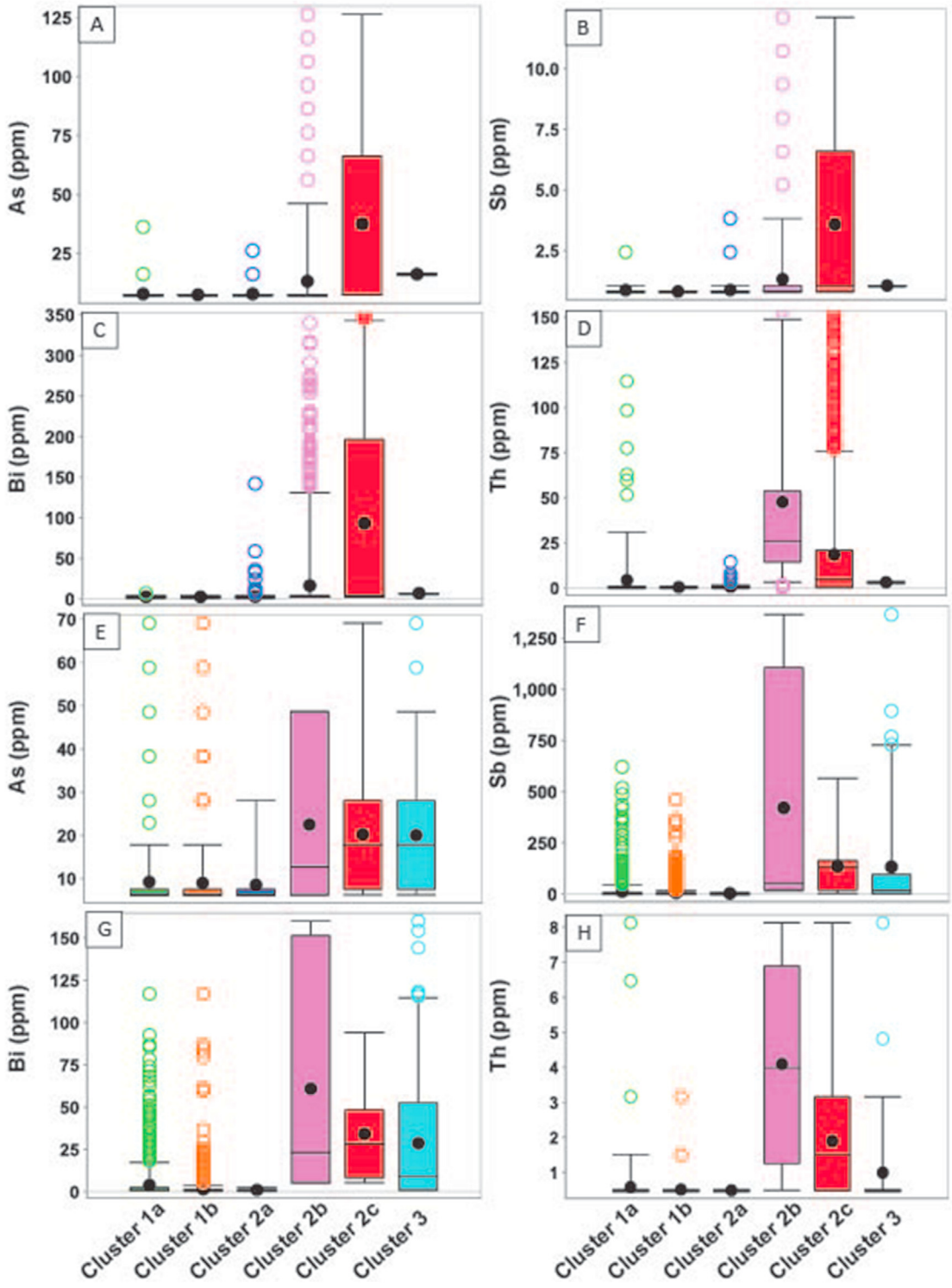

Fig. 12. Box and whisker plots for selected samples showing As, Sb, Bi and Th concentrations by epidote compositional clusters identified in this study. These elements were excluded from PCA and K-means clustering due to the abundance (>40%) of below detection limit values: A – D; Sample YE16AA063; and E–H: Sample YE16AA001.

et al., 2019), which indicates that host rock is unlikely to be the source of high concentrations of Pb and Mn in this type of epidote. However, Triassic volcanic rocks in the Ann Mason fault block (adjacent to sample YE16AA112) have nearly an order of magnitude higher concentrations of Mn and Pb than Jurassic intrusive rocks (Proffett and Dilles, 2008), and may be the source the for these elements in epidote from sample YE16AA112.

4.2. *Refining the number of unsupervised clusters*

Principal component maps of raster data presented in the current study highlight geochemically unique microscale textural features in epidote, such as growth and sector zones, by maximising the chemical differences between data points (e.g., YE16AA096; Fig. 6). In contrast, the clustering stage groups these textural domains to better capture

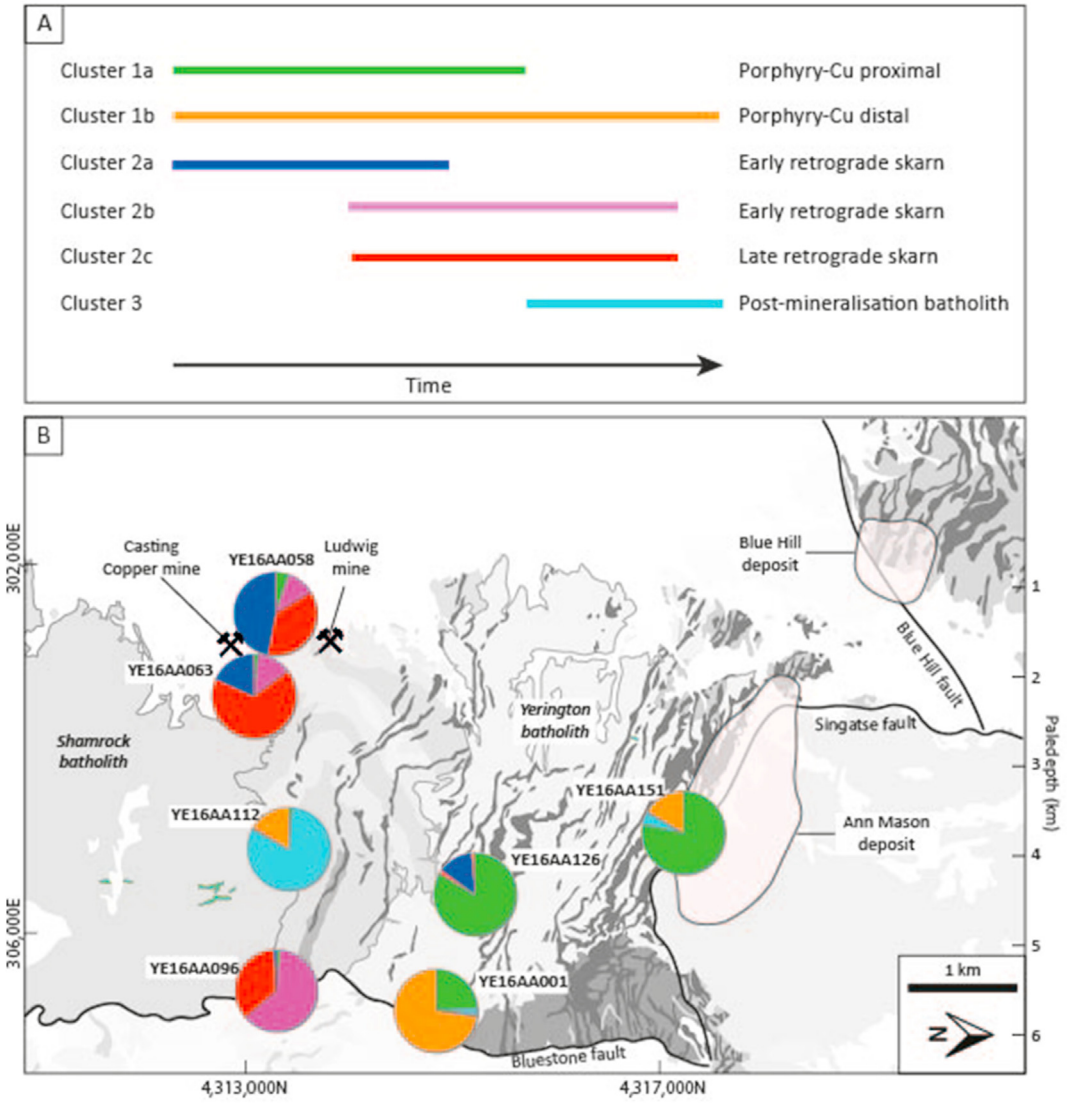

Fig. 13. A. Geology map of the Ann Mason fault block (colour map shown in Fig. 1), modified from Proffett and Dilles (1984), showing the spatial distribution of epidote compositional clusters and the relative proportions of clusters in each sample. Cluster colours in Fig. 13A apply to 13B; and B. Generalised paragenetic sequence of different epidote compositions in the Yerington district based on textural relationships observed in LA-ICP-MS raster maps.

alteration chemistry overprinting different earlier growth zonation (Fig. 9A). Six clusters were determined for the case study data, as an optimal number to represent cluster similarity (Fig. 7). However, increasing or decreasing the number of clusters provides a rise or drop in the granularity of the geochemical domains, respectively.

4.3. Misclassification of data points and cluster algorithm selection

Data points on individual raster maps group dominantly into either one or two clusters, per map, with a small frequency of datapoints belonging to subordinate clusters (Figs. 9–11). Where two clusters exist in similar proportions, the element associations between clusters are similar. For example, sample YE16AA096 is composed mainly of clusters 2b and 2c (both dominated by elevated REE values; Fig. 9A; Table 3). However, in the same sample, 2.4% of the datapoints have been classified as clusters 1a and 2a (Fig. 8). These datapoints tend to be marginal to dominant clusters in multivariate space, and probably represent a multidimensional, geochemical edge effect.

The K-means algorithm works by minimising the sum of squares differences within each cluster (MacQueen, 1967; Jain, 2010). Natural groups of data that have non-spherical shape and variance are not optimal for K-means clustering. As well, clusters of similar size or number of datapoints are favoured. Therefore, cluster centroids are typically pulled towards larger, denser clusters. Elements included in PCA and K-means clustering of raster map data in this study can occur in epidote at variable concentrations ranging from ppm to wt.% (Sr, Mn, Fe, Ce, U, Pb; Frei et al., 2004).

Although there are at least 18 compositionally distinct epidote minerals (Franz and Liebscher, 2004) natural samples typically represent a solid-solution between multiple epidote group end-members. Clustering on this kind of anisotropic natural data can result in soft boundaries between clusters, as observed in the current study. While our results are clearly interpretable and relatable to regional geology there is value to considering different clustering algorithms on a case-by-case basis. In practice, clustering algorithm comparison and selection can readily be undertaken as per Templ et al. (2008).

5. Conclusions

Raster mineral maps created using LA-ICP-MS data can illustrate microscale compositional domains within mineral grains. The application of machine learning cluster analysis improves the interpretability of

these maps by quantifying geochemical domains and yielding results which are reproducible between users. Cluster results from multi-sample, mono-mineralic datasets can be assessed in the context of other samples, both in geochemical and geographical map space, thereby extending insight from microscopic scales to regional scales to better understand geological paragenesis of an area. Although epidote was used in this study, the workflow is directly transferable to any raster mineral chemistry data, such as for chlorite, pyrite, zircon, or apatite; minerals commonly used in vectoring and fertility studies.

Author credit statement

Ayesha Ahmed: Conceptualization, Methodology, Writing - original draft, Visualisation, Investigation, Data validation, Writing - review & editing, Shawn Hood: Conceptualization, Methodology, Investigating, Reviewing, Editing, David Cooke: Conceptualization, Supervision, Reviewing, Editing, Project administration, Funding requisition.

Declaration of competing interest

The authors declare that they have no known competing financial interests or personal relationships that could have appeared to influence the work reported in this paper.

Acknowledgements

The research presented here was part of the primary author's Ph.D. studies, funded by the Australian Mineral Industries Research Association Limited (AMIRA) International P1153 project, "Applying the explorer's toolbox to discover Cu, Au, and Mo deposits", an Australian postgraduate award, and an Australasian Institute of Mining and Metallurgy (AusIMM) Education Endowment Fund scholarship.

Particular thanks to Ivan Belousov at the University of Tasmania for acquisition of LA-ICP-MS raster map data on epidote. Thanks to Al Cuison at the University of Tasmania lapidary for sample preparation, and to Sandrin Feig and Karsten Goemann for assistance using SEM facilities at the University of Tasmania. Special thanks to Matt Cracknell and Paul Olin, University of Tasmania, for constructive discussions on the application of statistical methods to geochemical raster map data. Samples used in this study were collected with the field-assistance of Josh Phillips, Amos Garay and Angela Escolme, with permission from Hudbay Minerals (formerly Entrée Gold), Quaterra Resources, and Mason Valley Copper Properties. John Dilles, Dick Tosdal and Matt Cunningham provided valuable field context for epidote formation in the Yerington district. Drs Christopher Lawley, Michael Gazley and an anonymous reviewer are thanked for their constructive reviews.

Appendix A. Supplementary data

Supplementary data to this article can be found online at https://doi.org/10.1016/j.acags.2020.100036.

References

Ahmed, A.D., 2019. Epidote and Chlorite Mineral Chemistry from the Yerington Porphyry Copper District, USA — Genetic and Exploration Implications. Unpublished Ph.D. thesis, University of Tasmania, Hobart, Australia, p. 468p.

Ahmed, A.D., Hood, S.B., Gazley, M.F., Cooke, D.R., Orovan, E.A., 2019. Interpreting element addition and depletion at the Ann Mason porphyry-Cu deposit, Nevada, using mapped mass balance patterns. J. Geochem. Explor. 196, 81–94.

Ahmed, A.D., Fisher, L., Pearce, M., Escolme, A., Cooke, D.R., Howard, D., Belousov, I., 2020. A microscale analysis of hydrothermal epidote: implications for the use of laser ablation-inductively coupled plasma-mass spectrometry mineral chemistry in complex alteration environments. Econ. Geol. 115 (4), 793–811. https://doi.org/10.5382/econgeo.4705.

Aitchison, J., 1982. The statistical analysis of compositional data. J. Roy. Stat. Soc. B 44, 139–160.

Aitchison, J., 1986. The Statistical Analysis of Compositional Data. Chapman and Hall Ltd., London, p. 416.

Armbruster, T., Bonazzi, P., Akasaka, M., Bermanec, V., Chopin, C., Gieré, R., Heuss-Assbichler, S., Liebscher, A., Menchetti, S., Yuanming, P., 2006. Recommended nomenclature of epidote-group minerals. Eur. J. Mineral 18, 551–556.

Bence, P., Woodhead, J.D., Paton, C., Hergt, J.M., Hellstrom, J., Norris, C.A., 2014. Towards a method for quantitative LA-ICP-MS imaging of multi-phase assemblages: mineral identification and analysis correction procedures. Geostand. Geoanal. Res. 38, 253–263.

Campbell, G.P., Curran, J.M., Miskelly, G.M., Coulson, S., Yaxley, G.M., Grunsky, E.C., Cox, S.C., 2009. Compositional data analysis for elemental data in forensic science. Forensic Sci. Int. 188, 81–90.

Cannell, J., Cooke, D.R., Walshe, J.L., Stein, H., 2005. Geology, mineralization, alteration, and structural evolution of the el teniente porphyry Cu-Mo deposit. Econ. Geol. 100, 979–1003.

Chayes, F., 1960. On correlation between variables of constant sum. J. Geophys. Res. 65, 4185–4193.

Chiaradia, M., Schaltegger, U., Spikings, R., Wotzlaw, J., Ovtcharova, M., 2013. How accurately can we date the duration of magmatic-hydrothermal events in porphyry systems? – an invited paper. Econ. Geol. 108, 565–584.

Cooke, D.R., Hollings, P., Wilkinson, J.J., Toasdal, R.M., 2014a. Geochemistry of Porphyry Deposits: Treatise on Geochemistry, second ed., vol. 13, pp. 357–381

Cooke, D.R., Baker, M., Hollings, P., Sweet, G., Chang, Z., Danyushevsky, L., Gilbert, S., Zhou, T., White, N.C., Gemmell, J.B., 2014b. New advances in detecting the distal geochemical footprints of porphyry systems—epidote mineral chemistry as a tool for vectoring and fertility assessments. Econ. Geol. Spec. Publ. 18, 127–152.

Demšar, J., Curk, T., Erjavec, A., Gorup, Č., Hočevar, T., Milutinovič, M., Možina, M., Polajnar, M., Toplak, M., Starič, A., Štajdohar, M., 2013. Orange: data mining toolbox in Python. J. Mach. Learn. Res. 14 (1), 2349–2353.

Dilles, J.H., 1987. Petrology of the Yerington Batholith, Nevada; evidence for evolution of porphyry copper ore fluids. Econ. Geol. 82, 1750–1789.

Dilles, J.H., Wright, J.E., 1988. The chronology of early Mesozoic arc magmatism in the Yerington district of western Nevada and its regional implications. Geol. Soc. Am. Bull. 100, 644–652.

Dilles, J.H., Einaudi, M.T., 1992. Wall-rock alteration and hydrothermal flow paths about the Ann-Mason porphyry copper deposit, Nevada; a 6-km vertical reconstruction. Econ. Geol. 87, 1963–2001.

Ding, C., He, X., 2004. K-means clustering via principal component analysis. In: International Conference on Machine learning, 21st, 2004, Banff, Canada, Conference Proceedings, p. 29.

Filzmoser, P., Hron, K., Reimann, C., 2009. Principal component analysis for compositional data with outliers: Environmetrics. Off. J. Int. Environ. Soc. 20, 621–632.

Franz, G., Liebscher, A., 2004. Physical and chemical properties of the epidote minerals–an introduction. Rev. Mineral. Geochem. 56, 1–81.

Frei, D., Liebscher, A., Franz, G., Dulski, P., 2004. Trace element geochemistry of epidote minerals. Rev. Mineral. Geochem. 56, 553–605.

Garwin, S., 2002. The Geologic Setting of Intrusion-Related Hydrothermal Systems Near the Batu Hijau Porphyry Copper-Gold Deposit, vol. 9. Society of Economic Geologists Special Publication, Sumbawa, Indonesia, pp. 333–366.

Gazley, M., Collins, K., Roberston, J., Hines, B., Fisher, L., McFarlane, A., 2015. Application of principal component analysis and cluster analysis to mineral exploration and mine geology [Ext. Abs]: AusIMM New Zealand Branch Annual Conference. In: Conference Proceedings, pp. 131–139. Wellington, New Zealand, 2015.

Gourcerol, B., Kontak, D.J., Thurston, P.C., Petrus, J.A., 2018a. Results of LA-ICP-MS sulfide mapping from Algoma-type BIF gold systems with implications for the nature of mineralizing fluids, metal sources, and deposit models. Miner. Deposita 53 (6), 871–894.

Gourcerol, B., Kontak, D.J., Thurston, P.C., Petrus, J.A., 2018b. Application of LA-ICP-MS sulfide analysis and methodology for deciphering elemental paragenesis and associations in addition to multi-stage processes in metamorphic gold settings. Can. Mineral. 56 (1), 39–64.

Grunsky, E.C., Mueller, U.A., Corrigan, D., 2014. A study of the lake sediment geochemistry of the Melville Peninsula using multivariate methods: applications for predictive geological mapping. J. Geochem. Explor. 141, 15–41.

Gustafson, L.B., Hunt, J.P., 1975. The porphyry copper deposit at El Salvador, Chile. Econ. Geol. 70, 857–912.

Hemley, J., Hunt, J., 1992. Hydrothermal ore-forming processes in the light of studies in rock-buffered systems; II, Some general geologic applications. Econ. Geol. 87, 23–43.

Hood, S.B., Cracknell, M.J., Gazley, M.F., 2018. Linking protolith rocks to altered equivalents by combining unsupervised and supervised machine learning. J. Geochem. Explor. 186, 270–280.

Huyck, H.L.O., 1989. When is a metalliferous black shale, not a black shale? US Geol. Surv. Circular 1058, 42–56.

Jackson, J.E., 2005. A User's Guide to Principal Components. John Wiley & Sons, New York.

Jain, A.K., 2010. Data clustering: 50 years beyond K-means. Pattern Recogn. Lett. 31, 651–666.

Jochum, K.P., Wilson, S.A., Abouchami, W., Amini, M., Chmeleff, J., McDonough, W.F., Raczek, I., Rudnick, R.L., Stoll, B., Tonarini, S., 2008. USGS GSD-1G: A Geological Reference Glass for in Situ Elemental and Isotopic Analysis. American Geophysical Union, Fall Meeting 2008.

Johnson, R., Wichern, D., 2007. Applied Multivariate Statistical Analysis. Prentice Hall International Inc, New Jersey.

Kerr, M.J., Hanley, J.J., Kontak, D.J., Morrison, G.G., Petrus, J., Fayek, M., Zajacz, Z., 2018. Evidence of upgrading of gold tenor in an orogenic quartz-carbonate vein

system by late magmatic-hydrothermal fluids at the Madrid Deposit, Hope Bay Greenstone Belt, Nunavut, Canada. Geochem. Cosmochim. Acta 241, 180–218.
Knopf, A., 1918. Geology and Ore Deposits of the Yerington District, Nevada. US Government Printing Office, p. 68.
Large, R.R., Danyushevsky, L., Hollit, C., Maslennikov, V., Meffre, S., Gilbert, S., Bull, S., Scott, R., Emsbo, P., Thomas, H., 2009. Gold and trace element zonation in pyrite using a laser imaging technique: implications for the timing of gold in orogenic and Carlin-style sediment-hosted deposits. Econ. Geol. 104, 635–668.
Lawley, C.J.M., Petts, D.C., Jackson, S.E., Zagorevski, A., Pearson, D.G., Kjarsgaard, B.A., Savard, D., Tschirhart, V., 2020. Precious Metal Mobility during Serpentinization and Breakdown of Base Metal Sulphide. Lithos, pp. 354–355.
MacQueen, J., 1967. Some methods for classification and analysis of multivariate observations: berkeley symposium on mathematical statistics and probability, 5th, 1967. In: Conference Proceedings, pp. 281–329.
Martín-Fernández, J.A., Hron, K., Templ, M., Filzmoser, P., Palarea-Albaladejo, J., 2012. Model-based replacement of rounded zeros in compositional data: classical and robust approaches. Comput. Stat. Data Anal. 56, 2688–2704.
Pan, Y., Fleet, M.E., 1990. Halogen-bearing allanite from the White River gold occurrence, Hemlo area, Ontario. Can. Mineral. 28, 67–75.
Papunen, H., Lindsjö, O., 1972. Apatite, monazite and allanite; three rare earth minerals from Korsnäs, Finland. Analysis 100, 133.
Parbhakar-Fox, A., Fox, N., Jackson, L., 2016. Geometallurgical evaluations of mine waste–an example from the Old Tailings Dam. In: 3rd AusIMM International Geometallurgy Conference 2016, 2016, pp. 193–204. Savage River, Tasmania.
Proffett, J.M., Dilles, J.H., 1984. Geologic Map of the Yerington District, Nevada, vol. 77. Nevada Bureau of Mines and Geology Map scale 1:24,000, 1 sheet.
Proffett, J.M., Dilles, J.H., 2008. Lower Mesozoic sedimentary and volcanic rocks of the Yerington region, Nevada, and their regional context. In: Wright, J.E., Shervais, J.W. (Eds.), Ophiolites, Arcs, and Batholiths: A Tribute to Cliff Hopson: Special Paper 438, vol. 438. Geological Society of America, pp. 251–288.
Quinby-Hunt, M.S., Wide, P., Berry, W.B.N., 1989. Element geochemistry of low calcic black shales—statistical comparison with other shales. US Geol. Surv. Circular 1037, 8–15.
Raimondo, T., Payne, J., Wade, B., Lanari, P., Clark, C., Hand, M., 2017. Trace element mapping by LA-ICP-MS: assessing geochemical mobility in garnet. Contrib. Mineral. Petrol. 172, 1.
Román, N., Reich, M., Leisen, M., Morata, D., Barra, F., Deditius, A.P., 2018. Geochemical and micro-textural fingerprints of boiling in pyrite. Geochem. Cosmochim. Acta 246, 60–85.
Reyes, A.G., 1990. Petrology of Philippine geothermal systems and the application of alteration mineralogy to their assessment. J. Volcanol. Geoth. Res. 43, 279–309.
Rudnick, R., Gao, S., 2014. Composition of the continental crust. In: Holland, H.D., Turekian, K.K. (Eds.), Treatise on Geochemistry. Elsevier, Oxford, pp. 1–51.
Sillitoe, R.H., 2010. Porphyry copper systems. Econ. Geol. 105, 3–41.
Smith, M.P., Henderson, P., Jeffries, T., 2002. The formation and alteration of allanite in skarn from the Beinn an Dubhaich granite aureole, Skye. Eur. J. Mineral 14, 471–486.
Sterk, R., Gazley, M.F., Wood, M.P., Collins, K.S., Collis, G., 2018. Maximising the value of Portable XRF data in exploration: an example from Marirongoe, Mozambique. Geochem. Explor. Environ. Anal. 18, 142–154.
Templ, M., Filzmoser, P., Reimann, C., 2008. Cluster analysis applied to regional geochemical data: problems and possibilities. Appl. Geochem. 23, 2198–2213.
Ubide, T., McKenna, C.A., Chew, D.M., Kamber, B.S., 2015. High-resolution LA-ICP-MS trace element mapping of igneous minerals: in search of magma histories. Chem. Geol. 409, 157–168.
Ulrich, T., Kamber, B.S., Jugo, P.J., Tinkham, D.K., 2009. Imaging element-distribution patterns in minerals by laser ablation–inductively coupled plasma–mass spectrometry (LA–ICP–MS). The Canadian Mineralogist v 47 (5), 1001–1012, 2009.
Wagstaff, K., Cardie, C., Rogers, S., Schrödl, S., 2001. Constrained k-means clustering with background knowledge: international conference on machine learning. In: 18th, Massachusetts, USA, 2001, Conference Proceedings, pp. 577–584.
Zhu, Z.-Y., Cook, N., Yang, T., Ciobanu, C., Zhao, K.-D., Jiang, S.-Y., 2016. Mapping of sulfur isotopes and trace elements in sulfides by LA-(MC)-ICP-MS: potential analytical problems, improvements and implications. Minerals 6, 110.